International Journal of Nanomedicine

Dovepress
Taylor & Francis Group

Open Access Full Text Article

ORIGINAL RESEARCH

Evaluation of Self-Illuminating Nanoconjugates Against Pancreatic Ductal Adenocarcinoma

Marcelina Abal-Sanisidro[1–3], Laura Ruiz-Cañas[4,5], Sandra Batres-Ramos[4,5], Miguel G Blanco[2,6], Maria Laura García-Bermejo[7], Jenifer García-Fernández[1], Luis Rodríguez-Cobo[8,9], Jose Miguel López-Higuera[8–10], Bruno Sainz Jr[3–5], María de la Fuente[1,3,11]

[1]Nano-Oncology and Translational Therapeutics Group, Health Research Institute of Santiago de Compostela (IDIS), University Clinical Hospital (CHUS), SERGAS, Santiago de Compostela, A Coruña, 15706, Spain; [2]Department of Biochemistry and Molecular Biology, University of Santiago de Compostela (USC), Santiago de Compostela, A Coruña, 15782, Spain; [3]Biomedical Research Networking Center on Oncology (CIBERONC), Instituto de Salud Carlos III, Madrid, 28029, Spain; [4]Department of Cancer Biology, Instituto de Investigaciones Biomédicas Sols-Morreale (IIBM), CSIC-UAM, Madrid, 28029, Spain; [5]Cancer, Area 3-Instituto Ramon y Cajal de Investigación Sanitaria (IRYCIS), Madrid, 28034, Spain; [6]DNA Repair and Genome Integrity Laboratory, CIMUS, University of Santiago de Compostela, (USC), Santiago de Compostela, A Coruña, 15706, Spain; [7]Biomarkers and Therapeutic Targets Group, Instituto Ramon y Cajal de Investigación Sanitaria (IRYCIS), Madrid, 28034, Spain; [8]Photonics Engineering Group, Universidad de Cantabria, Santander, Cantabria, 39005, Spain; [9]Biomedical Networking Research Center of Bioengineering, Biomaterials and Nanomedicine (CIBER-BBN), Instituto de Salud Carlos III, Madrid, 28029, Spain; [10]Instituto de Investigación Sanitaria Valdecilla (IDIVAL), Santander, Cantabria, 39011, Spain; [11]DIVERSA Technologies S.L., Edificio Emprendia, Santiago de Compostela, A Coruña, 15782, Spain

Correspondence: María de la Fuente, Nano-Oncology and Translational Therapeutics Unit, Health Research Institute of Santiago de Compostela (IDIS), University Clinical Hospital (CHUS), Building C, Floor −2, Lab 20, Travesía da Choupana s/n, Santiago de Compostela, ES15706, Spain, Tel +34 981 955 916, Email maria.de.la.fuente.freire@sergas.es

Introduction: Pancreatic ductal adenocarcinoma (PDAC) is expected to become the second leading cause of cancer-related mortality by 2030, underscoring the need for new therapeutic approaches. While photodynamic therapy (PDT) has proven to be efficient for treating superficial solid tumors, conventional laser-dependent PDT is limited by poor tissue penetration. To address this challenge, we developed a novel self-illuminating nanoconjugate platform (SI-NCs) capable of activating PDT without external light.

Methods: We engineered SI-NCs composed of the bioluminescent enzyme RLuc8 conjugated to quantum dots (QDots 705) to generate internal light for activating the FDA-approved photosensitizer verteporfin. We then evaluated SI-NC photophysical properties and assessed their ability to induce localized antitumor activity in PDAC models.

Results: SI-NCs were successfully synthesized and characterized, demonstrating efficient bioluminescence resonance energy transfer and activation of verteporfin. In vitro studies in immortalized pancreatic cancer cell lines and patient-derived primary cultures revealed the mechanism of action and confirmed antitumor efficacy of bioluminescent-activated PDT.

Conclusion: In vivo testing in patient-derived xenograft (PDX) models validated the therapeutic potential of SI-NCs, supporting this self-illuminating platform as a promising strategy to overcome light-penetration barriers and enhance PDT for PDAC treatment.

Keywords: photodynamic therapy, RLuc8-QDots nanoconjugates, BRET, pancreatic cancer, photosensitizer, ROS-responsive therapy

Introduction

Pancreatic ductal adenocarcinoma (PDAC) accounts for more than 90% of pancreatic cancer cases and is currently the fourth leading cause of cancer-related death worldwide,[1,2] with a five-year survival rate of approximately 11%.[1] The particular anatomical location and pathological features of PDAC make it one of the most difficult tumors to diagnose and treat. Even surgically resected patients present an average survival of only 10 to 20 months.[3] Moreover, the incidence and mortality of PDAC are rising each year, and PDAC is projected to become the second leading cause of cancer-related deaths in the US and Europe by 2030.[4,5] Therefore, the development of new, effective therapies for this devastating tumor is a healthcare priority.[6,7]

Photodynamic therapy (PDT) has emerged as a promising alternative to treat many different types of tumors.[8,9] PDT is based on a non-invasive approach to selectively eliminate cancer cells with minimal harm to surrounding healthy tissue via light irradiation.[10–12] PDT relies on the activation of photosensitizing (PS) agents by light at specific wavelengths, generating singlet

https://doi.org/10.2147/IJN.S545161
Received: 1 July 2025
Accepted: 22 December 2025
Published: 28 April 2026

Graphical Abstract

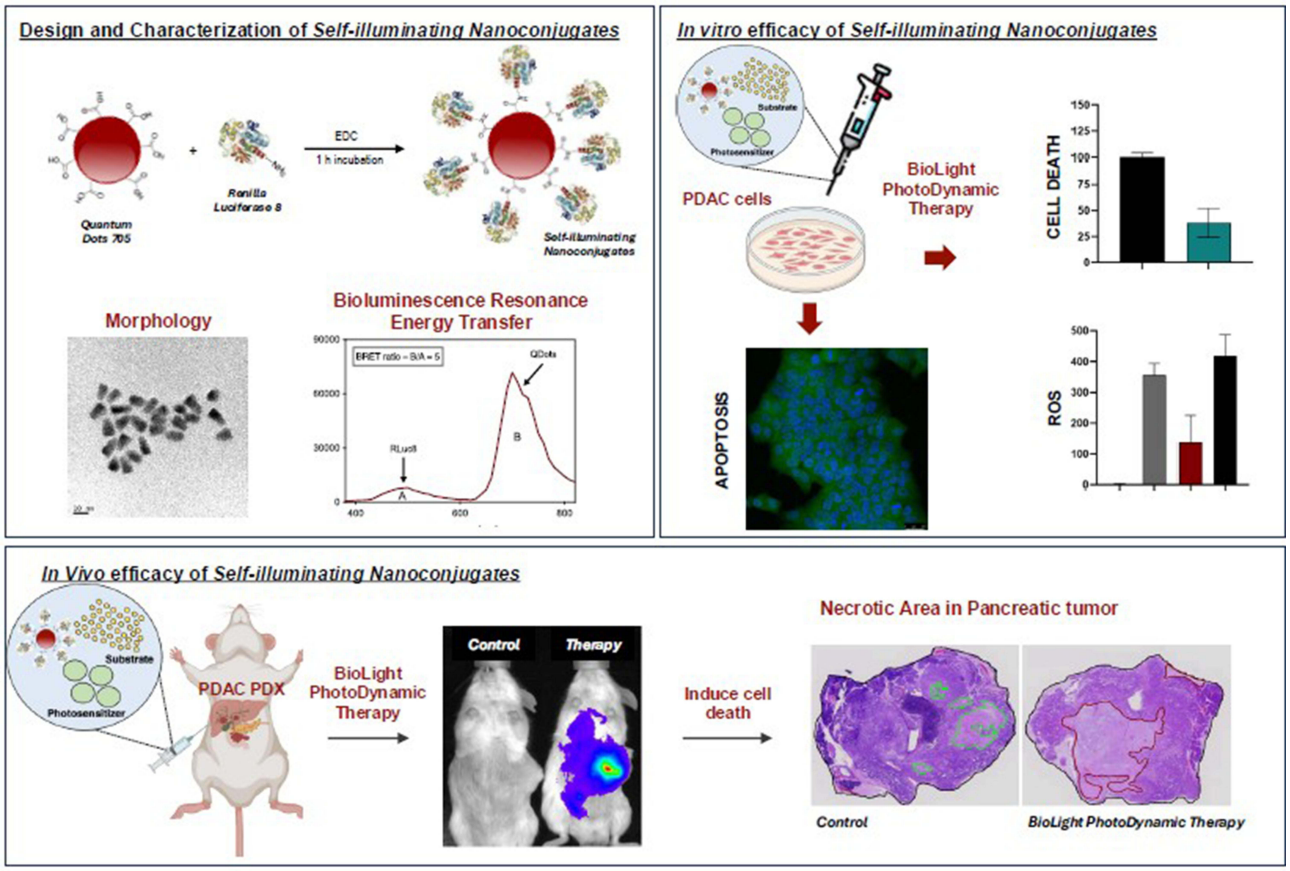

oxygen ($^3O_2 \rightarrow {}^1O_2$) and other reactive oxygen species (ROS) that induce oxidative damage and subsequent cell death.[13–15] This process can modulate immune responses via hypochlorous acid (HOCl) and trigger apoptosis through both intrinsic and extrinsic pathways, involving mechanisms such as caspase activation, oxidative stress, protein misfolding, and p38 MAPK activation. The precise mode of cell death depends on the intracellular localization of the PDT-induced oxidative stress.[7]

Despite its potential, traditional PDT faces significant limitations when treating deep-seated tumors like PDAC.[16,17] Light penetration is poor in deep tissues, especially at shorter wavelengths, while longer wavelengths produce less ROS.[8,17] The so-called "tissue optical window" (600–1200 nm) is optimal for PDT, but endogenous chromophores in tissue compete for light absorption.[18,19] As a result, current PDT techniques are largely restricted to superficial or endoscopically accessible tumors. Furthermore, PDAC's dense fibrotic stroma impedes both light penetration and drug delivery.[20,21] To overcome these general and PDAC-specific barriers, recent advances have explored internal light sources as a way of generating light within the tumor.[22,23]

Nanoparticles offer a promising strategy to improve PDT in deep tumors like PDAC, due to ability to accumulate in the tumor.[12,24] Quantum dots (QDots), in particular, are fluorescent nanoparticles known for their optical stability and prolonged emission after light excitation.[25,26] Their self-illuminating potential is enhanced when conjugated with Renilla luciferase (RLuc8), a bioluminescent protein.[27,28] Upon addition of the substrate coelenterazine (CTZ), light produced by RLuc8 can be transferred to QDots via Bioluminescence Resonance Energy Transfer (BRET).[27] These self-illuminating nanoconjugates (SI-NCs) have already demonstrated their potential for in vitro and in vivo imaging of C6 glioma live cells.[27] Likewise, Hsu et al[29] proposed the use of SI-NCs for treating A549 tumor cells, confirming improved tumor death in comparison with the application of an external light source. The superiority of this approach with respect to external laser

sources was also confirmed by Kim et al,[30] using in this case CT26 murine colon cancer, Murine Lewis lung cancer (LLC) and B16F10 melanoma cells. SI-NCs have additionally been investigated for antimicrobial applications.[31]

In this work, we propose the use of SI-NCs for the treatment of PDAC. We optimized the conjugation of RLuc8 to QDots 705, which are compatible with the FDA-approved photosensitizer verteporfin (marketed as Visudyne®). Verteporfin, approved for age-related macular degeneration, is known to inhibit angiogenesis following light activation.[32–34] Although clinical trials are investigating its use in cancer treatment, current protocols require invasive procedures to deliver external light to activate verteporfin.[35,36] SI-NCs present a minimally invasive alternative, capable of activating verteporfin internally through bioluminescence.

Importantly, verteporfin emits red light, which penetrates tissue more effectively than shorter wavelengths.[8,17,32,37] Related photosensitizers, such as the same PS family member, chlorin e6 (Ce6), have shown efficacy in SW480 colon cancer cells and ROS-responsive nanoparticles co-loaded with sorafenib, enhancing antitumor activity.[38,39]

Here, we introduce a novel type of SI-NCs specifically engineered to activate verteporfin and enable bioluminescence-driven PDT (BioLight PDT or BL-PDT) in PDAC. Our results provide strong evidence that this approach can overcome the limitations of conventional laser-based PDT and offer a promising new direction for PDAC treatment.

Material and Methods

Preparation of Self-Illuminating Nanoconjugates (RLuc8-Quantum Dots 705 Nanoconjugates)

To associate the purified RLuc8 protein (supp. Info.; "Extraction, purification and characterization of RLuc8") with the QDots, a previously described protocol was followed with some modifications.[28] Ten pmol of QDots 705, 400 pmol of RLuc8, and 40,000 pmol of EDC (N-(3-Dimethylaminopropyl)-N′-ethylcarbodiimide, Sigma-Aldrich, Spain) were combined, and the mixture was brought to a final volume of 20 µL in 10 mM PBS buffer (pH 7.4) and incubated at room temperature for 1 hour. The purification of the SI-NCs was carried out using spin filters (Amicon® Ultra Centrifugal Filters, 0.5 mL, Merck) in a refrigerated microcentrifuge (5417R; Eppendorf). The spin filters were first pre-washed with NTA buffer (N′,N-bis-(carboxymethyl)-L-lysine, Sigma-Aldrich, Spain) at 6000×g for 5 min to reduce QDot loss during the process. The filters were then flushed with 10 mM PBS buffer (pH 7.4) at 6000×g for 5 min, and the conjugation reaction was transferred to the spin filters, and 200 µL of PBS was added and centrifuged for 3 min at 4°C and 3000×g. Four washes were then performed with 200 µL of PBS each, centrifuging as described above. Finally, SI-NCs were collected in 20 µL of PBS buffer, centrifuged for 2 min at 4°C and 1000×g. The reaction was escalated 5-fold to ease future experiments without compromising its physicochemical properties.

Evaluation of Self-Illuminating Nanoconjugates

To determine the efficacy of the conjugation, different samples, specifically i) free QDots, ii) a physical mixture of QDots and the EDC coupling reagent, and iii) the SI-NCs (RLuc8-QDots 705 nanoconjugates), prepared with 6X DNA orange loading buffer dye (Promega), were loaded in a 1% agarose gel (Fischer Scientific) in 1X TAE buffer. Electrophoresis was performed at 100V for 30 min, and the gel was visualized in a Chemidoc standard UV developer chamber (BioRad). In addition, a 12% acrylamide/bis-acrylamide (29:1) denaturing SDS-PAGE gel (BioRad) was prepared, and additional samples were loaded, specifically i) the naked protein RLuc8, ii) free QDots, and iii) SI-NCs. Electrophoresis was performed at 150V for 90 minutes. The gel was developed using Coomassie® Brilliant Blue staining (ThermoFisher Scientific, USA).

BRET phenomenon was tested after its activation with 1 µg of CTZ (ThermoFisher Scientific, USA) in a luminometer (SYNERGY H1, microplate reader, BioTek). The stability of the SI-NCs was determined by measuring their BRET kinetics at the time of production, as well as at days 4 and 7 post-production. The kinetics of the reaction were determined in duplicate in a 96-well plate, monitoring the bioluminescence reaction from time 0 min (addition of the substrate) to 3 hours, and taking measurements every 5 min.

Quantum Yield Determination

The quantum yield (or BRET yield), ie., the energy transferred within the nanoconjugates, was calculated according to equation 1.

$$Qy = \frac{RLuc8\ Energy\ Coupled\ to\ the\ QD}{Energy\ Emitted\ by\ the\ QD}$$

The numerator was obtained by subtracting the emission of the free RLuc8 (in the same wavelength range that the SI-NCs would emit) from the emission of the RLuc8 already coupled to the QDots (SI-NCs).

Cell Culture Maintenance

The established and commercially available cell lines MiaPaCa-2, PANC-1, PaTu 8988t, PaTu 8988s and L3.6pl cells were cultured in RPMI 1640 media (Invitrogen, Cat no. 61870044) containing 10% fetal bovine serum and 50 units/mL penicillin/streptomycin in a humidified incubator (5%) at 37°C, and cultures were tested for Mycoplasma periodically. The L3.6pl cell line (RRID:CVCL_0384) is a highly metastatic PDAC cell line, originally described by *Bruns* et al.[40]

Cellular Internalization Studies

For cellular internalization studies, 6×10^4 L3.6pl, MiaPaCa-2, PANC-1, PaTu 8988t or PaTu 8988s cells/ well were seeded in 8-chamber slide plates and incubated overnight. The following day, 2 pmol of SI-NCs were added to the wells and internalization was studied at different time points: 20 min, 1h and 3h. After incubation, treatments were removed, cell nuclei were stained with Hoechst 33342 (ThermoFisher, USA), cytoskeleton was stained with Alexa Fluor 488 Phalloidin™ (Invitrogen™) (only for 3D projections), cells were fixed with 4% PFA (ThermoFisher, USA), and cultures were observed by Confocal Laser Microscopy (CLM; Confocal Laser Microscopy Leica SP8®). Results were verified by Flow Cytometry (FACS Aria IIu de BD) in L3.6pl, MiaPaCa-2 and PANC-1 cells. 5×10^5 cells/well were seeded in 6-well plates and incubated overnight. Next, 10 pmol of the nanoconjugate treatments were added to the cells, and after incubation, cells were washed with 2X DPBS and fixed with 2% PFA.

Cell Viability Assays

For cytotoxicity studies, L3.6pl, MiaPaCa-2 and PANC-1 cells were seeded in 96-well plates at a density of 2.5×10^3 cells/well and incubated for 24h. To determine the toxicity of the photosensitizer and the SI-NCs, each was tested in separate experiments. Both were applied in increasing order of concentration and incubated for 4 hours. Cell viability was determined using the MTT assay (3-(4,5-dimethylthiazol-2-yl)-2,5-diphenyltetrazolium bromide, Alfa Aesar) and the colorimetric assay was read using a scanning multi-well plate reader at 570 nm (Multiskan EX, ThermoLabsystems®).

Experiments to determine cell viability after BL-PDT treatment *[BL-PDT = verteporfin (PS) + SI-NCs + substrate (CTZ)]* were also performed. At 24h post-seeding, SI-NCs were added to the cells at 1 pmol. Next, verteporfin (4 μM) was added and incubated for 2h. After treatments, cells were washed twice with 1X PBS. The photodynamic process was induced by adding 2 μg of CTZ to each well. After 12h, cytotoxicity was determined using the aforementioned MTT assay. The negative controls (0% cell death) consisted of cells growing in normal conditions and cells in which the vehicles were added. The positive control (100% cell death) consisted of cells treated with a solution of Triton 0.1% in DPBS.

Measurement of Reactive Oxygen Species Production and Apoptosis Induction

To determine the presence of intracellular ROS produced by the BL-PDT process, a fluorescence-based assay was performed, consisting of staining cells with the fluorescent dye 2′,7′-dichlorodihydrofluorescein diacetate (H_2DCFDA; ThermoFisher Scientific, USA), as per the manufacturer's instructions. Briefly, a 96-multiwell black-wall plate with clear bottoms was seeded with 2.5×10^3 cells/well and incubated for 24h. Cells were incubated with the dye at a final concentration of 5 μM for 60 min. Then, cells were treated with the same conditions and quantities of SI-NCs, verteporfin and CTZ, as mentioned in the previous section (*Cell viability assays*) and were incubated at 37°C for the PDT process. As a positive control, Luperox® (Sigma Aldrich, USA) was added at a concentration of 100 μM and incubated for 2h at 37°C. ROS generation was measured with a fluorimeter at an excitation wavelength of 485 nm and an emission of 535 nm. The H2DCFDA fluorescence was normalized against the assay's negative and positive controls to better reflect relative intracellular ROS levels under each treatment condition.

Laser-PDT culture conditions were the same as described in the previous paragraph. After treatment, cells were washed twice with PBS and laser-PDT was performed at different energy ratios in J/cm.[2] The optimal signal was used to compare with the BL-PDT.

Apoptosis after ROS production was evaluated by immunofluorescence-based detection of Annexin V. After BL-PDT treatment, cells were fixed with 4% PFA for 15 min, then incubated in 10% normal goat serum to block non-specific protein-protein interactions, followed by mouse monoclonal anti-annexin V (Abcam, NL) staining overnight at 4°C. Annexin V was observed with a Leica SP5 confocal laser microscope (Leica, Nussloch, Germany) using an excitation wavelength of 495 nm and an emission of 519 nm.

In vivo Studies

PDAC patient-derived xenografts (PDAC PDX Panc354 and PancA6L) were obtained from Dr. Manuel Hidalgo under a Material Transfer Agreement with the Spanish National Cancer Centre (CNIO), Madrid, Spain (Reference no. I409181220BSMH) and the use of these patient-derived material was approved by the CSIC institutional review board with number 329/2024. To establish low-passage primary PDAC PDX-derived in vitro cultures, xenograft tumors were minced, enzymatically digested with collagenase (Stem Cell Technologies) for 60 min at 37°C, clarified via multiple rounds of filter purification with 100 µm and 40 µM Fisherbrand™ Sterile Cell Strainers (FisherScientific, Cat no. 11517532 and 11587522), and after centrifugation for 5 min at 1800 rpm, the cell pellets were resuspended and cultured in RPMI (Invitrogen) supplemented with 10% FBS (Invitrogen), 50 units/mL penicillin/streptomycin and fungizone (Invitrogen). Primary cultures were tested for Mycoplasma at least every 4 weeks.

To perform PDT in vivo, 9-week-old 25 g male NOD.SCID (NOD.CB17-Prkdcscid/NCrHsd) mice (Janvier Labs, France) were orthotopically injected with 2×10^5 cells of the indicated PDX-derived cultures (resuspended in 50 µL MatrigelTM, BD Cat no. 354234) to form tumors. Fifteen mice were injected for each PDX-derived culture used. Approximately two weeks post-orthotopic injection, the photosensitizer Verteporfin (200 mg/kg) and SI-NCs (50 pmol) were administered intraperitoneally. Meanwhile, the substrate CTZ (20 µg) was administered by retro-orbital sinus injection in isoflurane-inhalation anaesthetized mice. The therapy workflow was as follows: first, photosensitizer was intraperitoneal (IP) administered and incubated for 1h; then, SI-NCs were injected, and after 30 minutes, the substrate (CTZ) was administered to induce BL-PDT. Mice were treated twice a week for 3 weeks. For the negative control group, PBS was injected. The sham (vehicle-control) group consisted of mice treated with the photosensitizer and the SI-NCs without the substrate addition (no BL-PDT treatment), and the therapy (positive-control) group consisted of mice treated with the complete BL-PDT treatment [BL-PDT = verteporfin (PS) + SI-NCs + substrate (CTZ)].

Immunohistochemistry Procedures

For histopathological analysis, 3 µm sections of FFPE blocks were stained with hematoxylin and eosin (H&E). Additional serial sections were used for immunohistochemical (IHC) analysis of PCNA. For PCNA, sections were incubated with anti-mouse-biotin 1:500 (DAKO, Cat no. E0354) for 45 min followed by ABC-HRP kit (Vectastain, Cat no. PK-6100) for 30 min at room temperature. Counterstaining was performed with hematoxylin. Digital Images were obtained using a digital scanner, "MOTIC EASY SCAN ONE" with a 20X Plan Apo objective (resolution of 0.22 µm/pixel). Digital images were analyzed and adjusted using ImageJ software.

TUNEL (TdT-Mediated dUTP Nick-End Labeling) Assay

Three-µm sections of formalin-fixed paraffin-embedded (FFPE) PDAC tumors were used for apoptosis detection by TUNEL assay (DeadEnd™ Fluorometric TUNEL System, PROMEGA), following the manufacturer's instructions. Briefly, tissues were de-paraffinized in fresh xylene, washed in 100% ethanol, rehydrated by sequential immersion through graded ethanol washes (100%, 95%, 85%, 70% and 50%) and fixed using 4% methanol-free formaldehyde in PBS. Tumor sections were then treated with proteinase K and incubated with the transferase enzyme and the fluorescein-12-dUTPs, at 37°C for 60 minutes, inside a humidified chamber. Slides were covered using an Anti-Fade solution (Molecular Probes), and the fluorescein-12-dUTP-labeled DNA was visualized using a Nikon Eclipse 200Ts fluorescence microscope (Izasa S.A., Barcelona, Spain). Images were captured with a microscope-associated camera and processed with a Nikon software package.

Statistical Analysis

Error bars represent standard deviation (s.d.) from the mean (at least n = 3 per group). Statistical analyses were performed with GraphPad Prism® Software (version 9.0). Data were analyzed by two-tailed Student's *t*-test to compare two experimental groups and one- or two-way analysis of variance (ANOVA) with a Tukey correction was used to calculate differences among multiple populations. P-values <0.05 were considered statistically significant. Statistical analyses meaning: * ($p < 0.05$), ** ($p < 0.01$), *** ($p < 0.001$) and **** ($p < 0.0001$).

Results and Discussion

To develop a PDT approach, triggered by BL-PDT and capable of inducing ROS in tumors in vivo, we developed SI-NCs composed of fluorescent metallic quantum dots (QDots 705) and the bioluminescent protein RLuc8, assembled via amine condensation to activate verteporfin (PS) (Figure 1a and b). RLuc8, a *Renilla* luciferase mutant purified following a previously described protocol with slight modifications[28] (Figure S1a and b), was selected for its high stability and enhanced light-emission properties[27] Upon activation with its substrate (CTZ), RLuc8 reaches a peak emission at 490 nm (Figure S1c).

To optimize the RLuc8-QDots 705 conjugation, we tested various buffer systems (PBS, HEPES, MES, and Tris-HCl). PBS (10 mM, with 0.1 M NaCl) was chosen for its ability to preserve protein integrity, reduce aggregation, and support favourable protein–protein interactions.[41,42] Tris-base was avoided due to its incompatibility with amine-involving reactions, which can result in lower yields.[43,44]

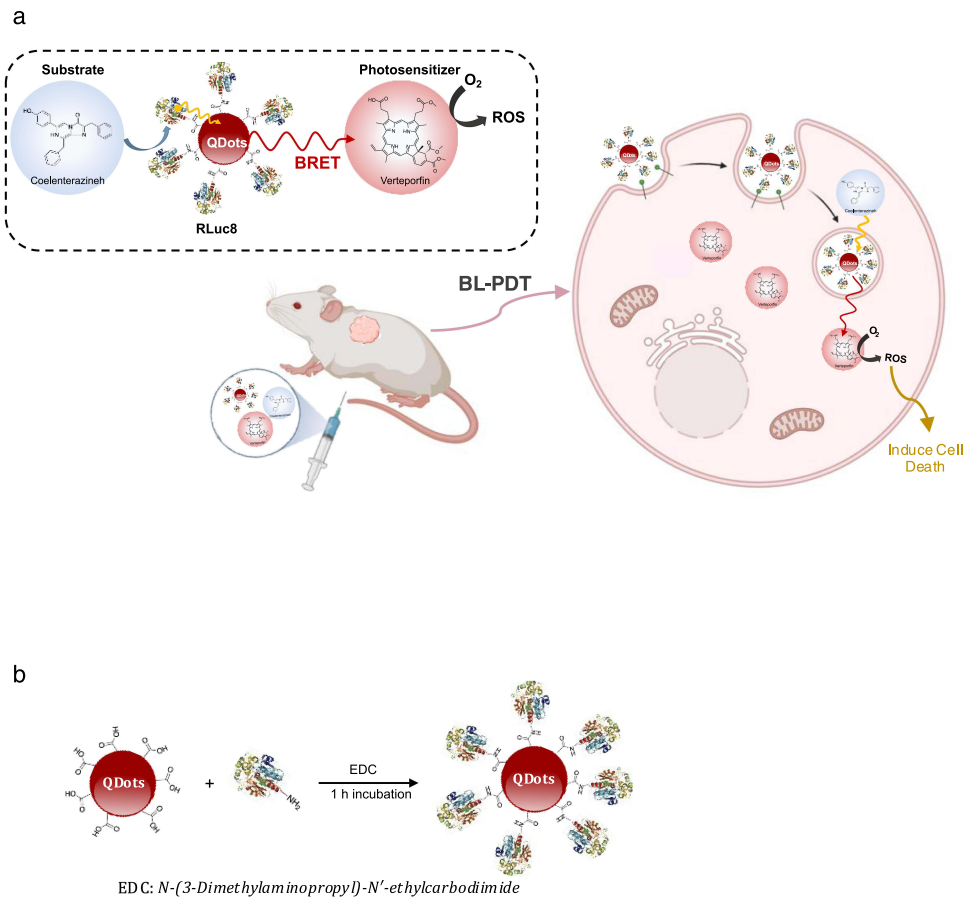

Figure 1 Preparation of SI-NCs (RLuc8-QDots 705 nanoconjugates). (**a**) Schematic representation of the proposed mechanism based on bioluminescent-activated (BioLight) photodynamic therapy (BL-PDT). In deep-tissue, SI-NCs BioLight source can excite a target photosensitizer drug more effectively than external laser light. (**b**) SI-NCs coupling reaction undergoes a conversion of the carboxylic acid to amide using EDC (N-(3-Dimethylaminopropyl)-N′-ethylcarbodiimide) as an activating agent.
Abbreviations: RLuc8, Luciferase enzyme; QDots, Quantum Dots; Substrate, Coelenterazine (CTZ); Photosensitizer, Verteporfin; BRET, Bioluminescence Resonance Energy Transfer; ROS, Reactive Oxygen Species; BL-PDT, BioLight Photodynamic Therapy.

Successful conjugation was confirmed by agarose gel electrophoresis,[28] which showed reduced electrophoretic mobility of SI-NCs compared to free QDots (Figure 2a), consistent with previous reports using QDot 655 nanoconjugates.[29] SDS-PAGE further validated conjugation: (i) free RLuc8 migrated at ~35 kDa, (ii) QDots did not enter the gel due to their size, and (iii) SI-NCs remained in the well, indicating increased molecular weight (Figure 2b).

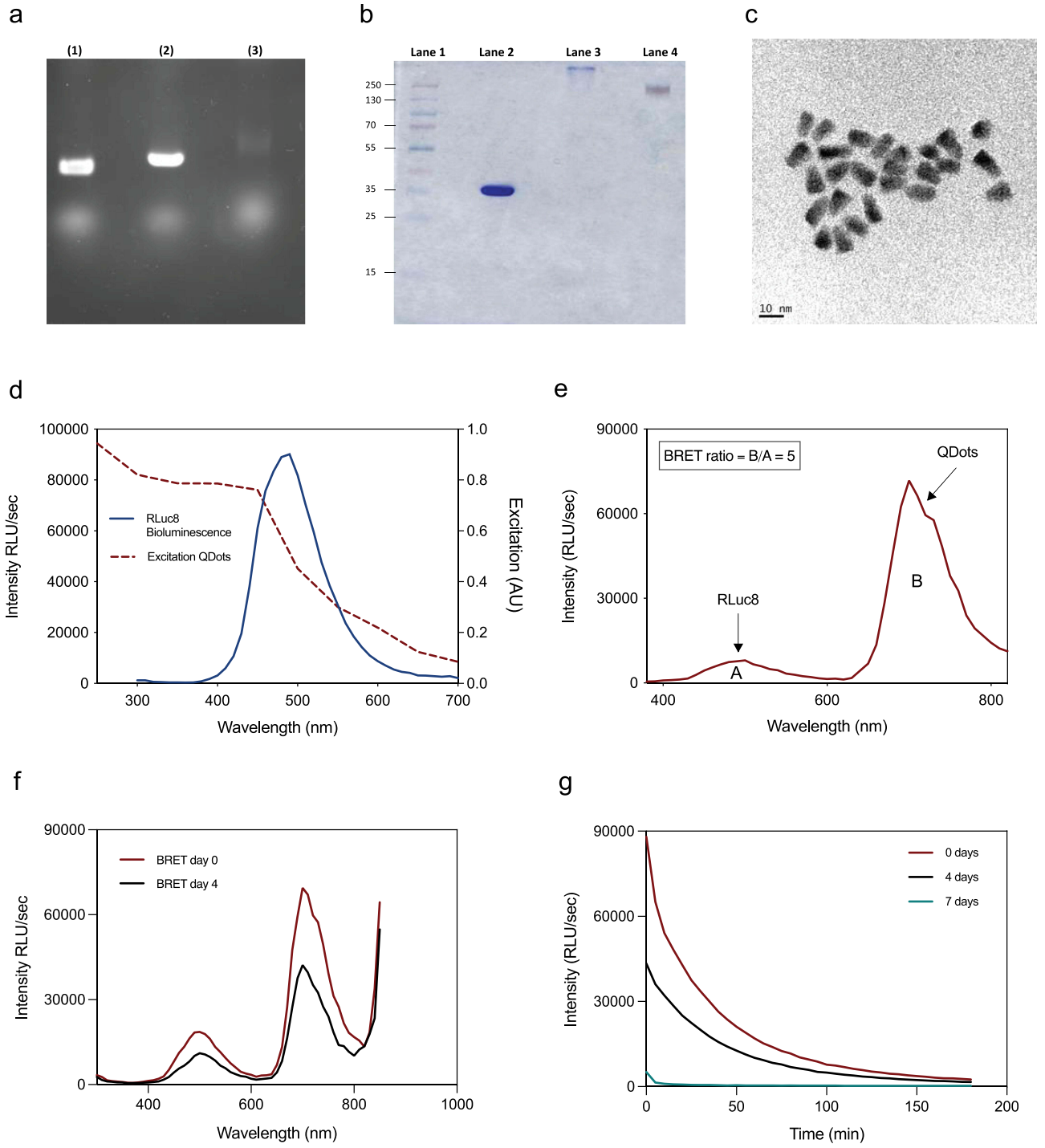

Figure 2 Characterization of SI-NCs. (**a**) 1% agarose gel containing the components: [(1) free QDots; (2) free QDots + EDC physical mixture; (3) SI-NCs], confirming successful nanoconjugate associations. (**b**) 12% acrylamide gel electrophoresis [Lane 1: ladder; Lane 2: naked RLuc8; Lane 3: SI-NCs; Lane 4: free QDots] (**c**) TEM image of SI-NCs morphology and particle size. Scale bar: 10 nm. (**d**) QDots excitation spectra overlap with the maximum enzyme RLuc8 emission peak. (**e**) SI-NCs emission spectrum (BRET spectral scanning) with CTZ (1 µg) addition. The BRET ratio was calculated from the ratio of the area under the curve of RLuc8 (**a**) emission between 395 and 600 nm and that of QDots (**b**) emission between 650 and 760 nm. (**f**) BRET scanning at day 0 and 4. (**g**) Kinetics of SI-NCs emission at 0, 4 and 7 days after their coupling.

https://doi.org/10.2147/IJN.S545161

Transmission electron microscopy (TEM) revealed that conjugation did not significantly alter QDot morphology or size, with conjugates averaging ~20 nm - similar to the commercial QDot size range (15–21 nm) (Figure 2c, S2a and b). Samples appeared homogeneous with a polydispersity index of <0.3. Dynamic Light Scattering (DLS) and Laser Doppler Anemometry (LDA) confirmed these findings and showed a negative surface charge, attributed to the QDot's lipophilic coating. Bradford assay estimated a high protein loading efficiency of 88%[45] (Table 1).

For efficient BL-PDT, optimal BRET between the SI-NCs and verteporfin is critical.[34–37] Since RLuc8 alone cannot directly transfer energy to the photosensitizer, QDots serve as intermediates. BRET operates on Förster resonance energy transfer principles, where efficiency depends on the inverse sixth power of the donor–acceptor distance and their relative orientation. Lack of BRET signal does not necessarily imply absence of interaction,[46–49] but effective energy transfer requires strong spectral overlap.[50–52]

In the SI-NCs, RLuc8 acts as the energy donor and the QDots 705 as the energy acceptor. Spectral analysis confirmed a strong overlap between RLuc8 emission and QDots excitation (Figure 2d), enabling effective energy absorption and transfer to activate verteporfin (QDot excitation/emission in Figure S2c). BRET scanning spectra revealed that a substantial portion of RLuc8's emission is absorbed by QDots (Figure S2d). The BRET ratio, calculated as the area under the acceptor curve divided by that of the donor, was 5.05 (Figure 2e),[50,51] significantly higher than the 1.32 reported by *So* et al for RLuc8-QDot 655 systems[27]. The highest BRET ratio occurs when the light intensity of the donor is closest to 0, indicating that almost all the bioluminescent activity is being transferred to the acceptor. Therefore, this enhanced ratio may result from differences in buffer composition, conjugation method,[53] or the improved stability and light output of RLuc8.

The SI-NCs also demonstrated a BRET quantum yield (Qy) of 0.64–0.72, exceeding previous reports of 0.60–0.65 for similar systems.[30] Ideally, if all donor emission were transferred to the acceptor, this value would approach 1.

We next assessed the stability of SI-NCs over time by tracking BRET kinetics at time 0, and after 4 and 7 days of storage at 4°C. On day 4, BioLight activity had declined by 50% (Figure 2f), and by day 7, BRET activity was no longer detectable (Figure 2g). While a complete loss of activity by day 4 was reported in earlier studies,[27,28] our formulation showed improved stability, highlighting its potential for further in vivo applications.

To evaluate the interaction of SI-NCs with pancreatic cancer cells, we conducted a series of in vitro experiments across multiple PDAC cell lines (Figure 3 and S3). To our knowledge, this is the first study assessing this type of SI-NC for potential pancreatic cancer treatment.[54]

We first examined internalization in L3.6pl cells, a pancreas-to-liver metastatic cancer cell line and in the MiaPaCa-2 PDAC cell line (Figure 3a–c). In both cases, SI-NCs were rapidly internalized, with visible uptake as early as 30 minutes and peak internalization achieved by 3 hours. This swift uptake may be advantageous for therapeutic applications in PDAC by minimizing drug degradation, bypassing drug resistance (a common issue in this tumor type), and reducing dosage and systemic toxicity, supporting safer and longer-term use.

Consistent results were obtained in additional PDAC lines, including PANC-1, PaTu8889t and PaTu8889s cells (Figure S3a–c). Quantitative analysis using flow cytometry confirmed high uptake rates: 93% of L3.6pl cells were positive after just 30 minutes (Figure 3d), with peak mean fluorescence at 2 hours. In MiaPaCa-2 cells, nearly 99% of cells were positive across all time points, with maximal fluorescence at 1 hour (Figure 3e). Similar uptake patterns were observed in PANC-1 cells (Figure S3d).

Table 1 Physicochemical Characterization of SI-NCs Measured by DLS and LDA. Percentage of RLuc8 Loaded to QDots 705 Quantified by Bradford's Assay (Results are Expressed as Mean ± Standard Deviation, n = 5)

Formulation	Size (nm)	PdI	ZP (mV)	% RLuc8
SI-NCs	22 ± 2	<0.3	− 6 ± 1	88 ± 2

Abbreviations: nm: nanometer, PdI: polydispersity index, ZP: zeta potential in millivolts (mV), SI-NCs: Self-Illuminating Nanoconjugates (RLuc8-QDots 705).

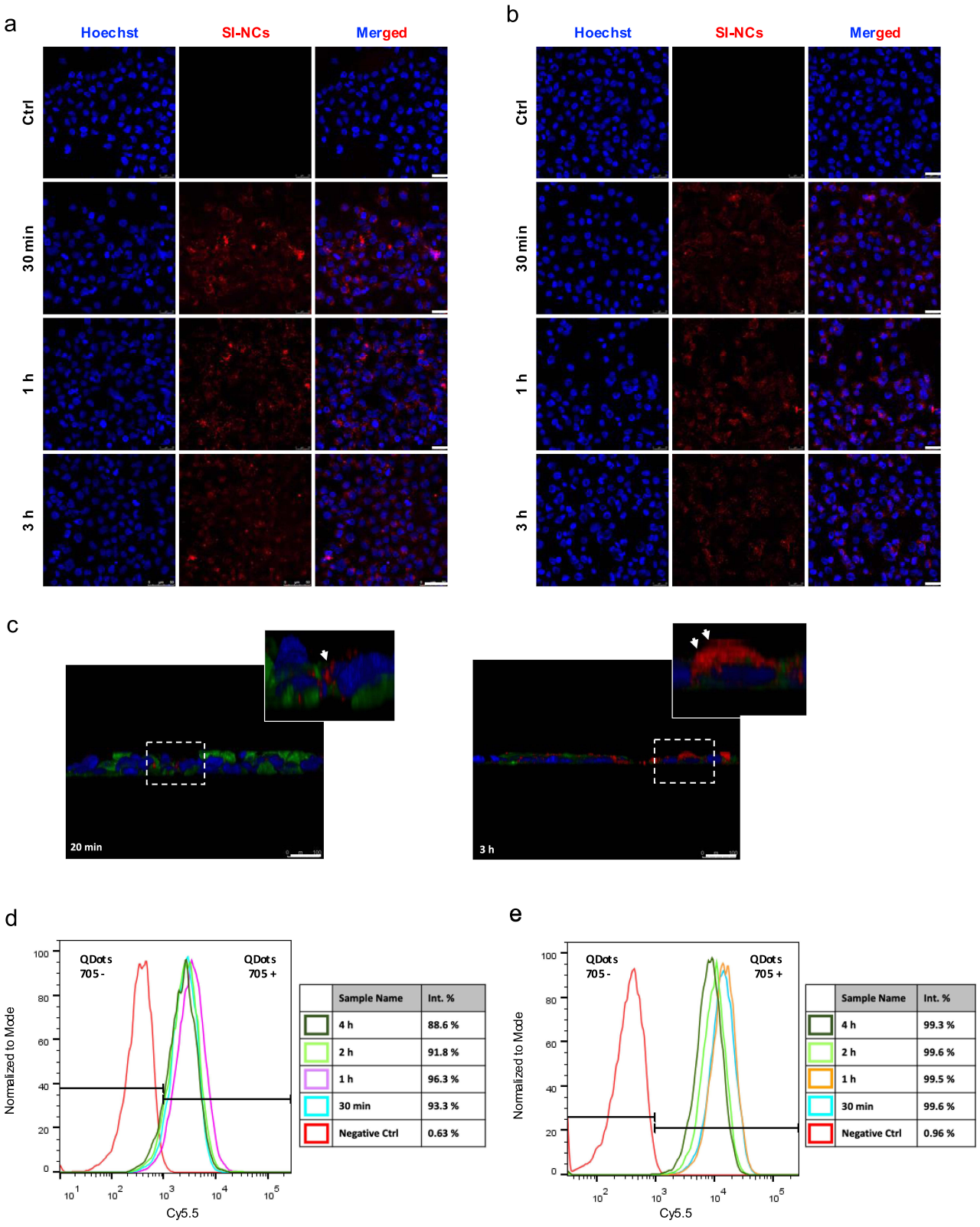

Figure 3 SI-NCs efficiently interact with PDAC cells. (**a**) Uptake experiments in the metastatic pancreas to liver cancer cell line L3.6pl and (**b**) the primary tumor cell line MiaPaCa-2 with SI-NCs (red signal), incubated across increasing time points (30 min to 3h). Untreated cells were used as a negative control. Cell nuclei were stained with Hoechst 33342 (blue signal) and observed by Confocal Laser Microscopy. (Scale bar: 25 μm, white) (**c**) 3D projections of Confocal images in L3.6pl cells. SI-NCs (red) are indicated with white arrows; cell nuclei were stained with Hoechst 33342 (blue); cytoskeleton (green) stained with Alexa Fluor 488 Phalloidin™ (Invitrogen™). Zoomed images represented in the white dotted square (Scale bar: 100 μm, white). Evaluation of Cy5.5 positive cells by flow cytometry to determine the internalization of SI-NCs (SI-NCs containing QDots 705 are observed by the Cy5.5 laser line). % Internalization and mean fluorescence expressed in tables (**d**) for L3.6pl and (**e**) for MiaPaCa-2 cells.

https://doi.org/10.2147/IJN.S545161

We further evaluated photosensitizer uptake by confocal microscopy in L3.6pl and MiaPaCa-2 cells using a 2 µM dose of verteporfin, up to 2 hours post-treatment (Figure 4a and b). These results are in line with previous studies reporting internalization times ranging from several minutes up to 3 hours for SI-NCs, and a standard 3-hour incubation for the photosensitizer alone.[29,30]

Importantly, SI-NCs also demonstrated efficient uptake in PDX-derived cultures, including Panc354 and PancA6L. However, as expected, internalization efficiency in primary cultures was generally lower than in established cell lines (data not shown), a known limitation in nanoparticle-based approaches.

Before assessing the therapeutic efficacy of BL-PDT in PDAC cells, we conducted preliminary studies with the photosensitizer (verteporfin) and QDots 705. An absorbance spectrum confirmed verteporfin's excitation peak at 690 nm (Figure 5a).

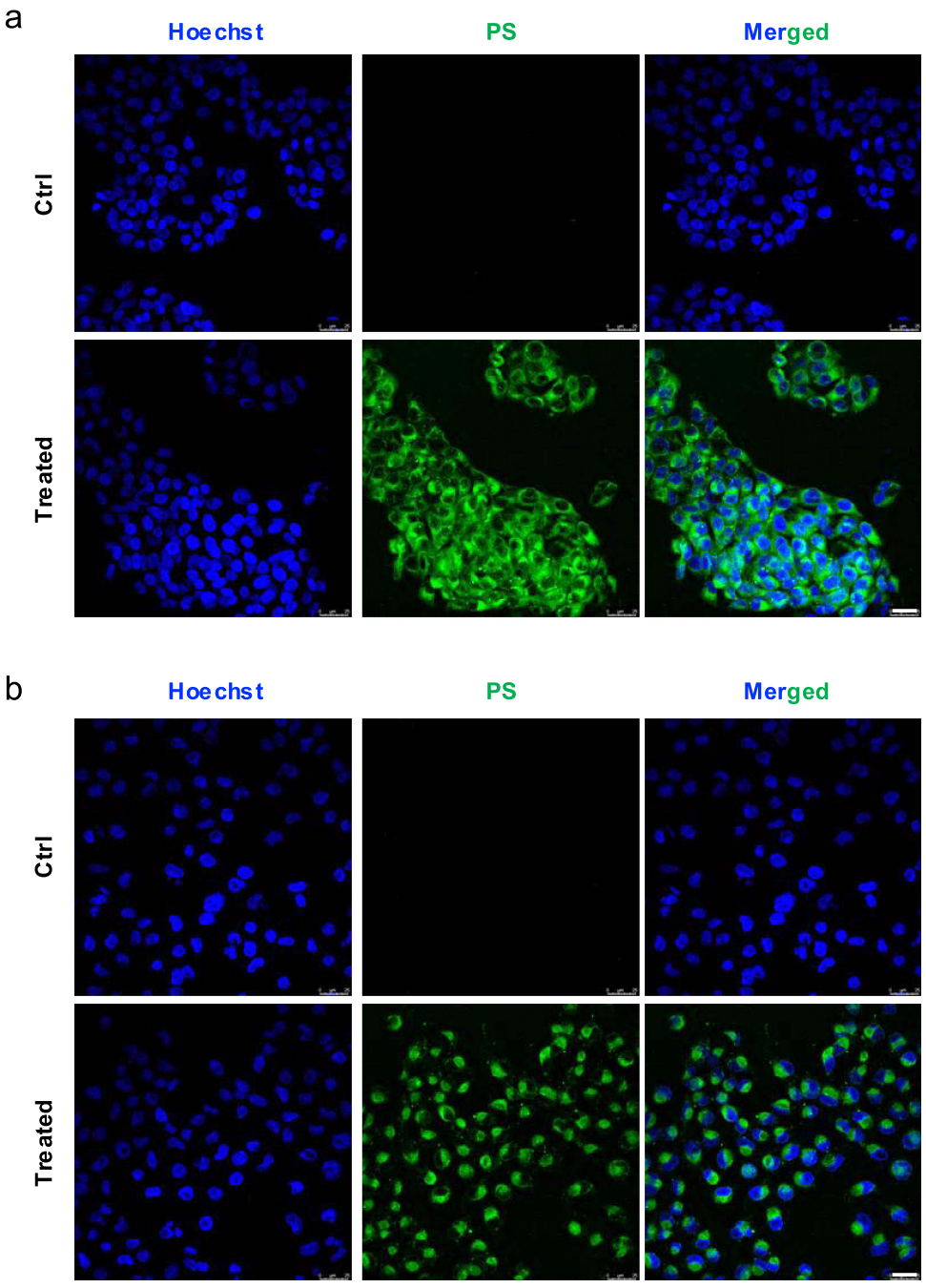

Figure 4 The photosensitizer verteporfin has an optimal cytosolic distribution in vitro. (**a**) L3.6pl and (**b**) MiaPaCa-2 cell cytosolic distribution of the photosensitizer. Images acquired by CLM after adding a dose of 2 µM and after a 2-hour incubation (Scale bar: 25 µm, white). Cell nuclei were visualized with Hoechst 33342 (blue signal) and the fluorescent photosensitizer cytosolic distribution is observed in green.

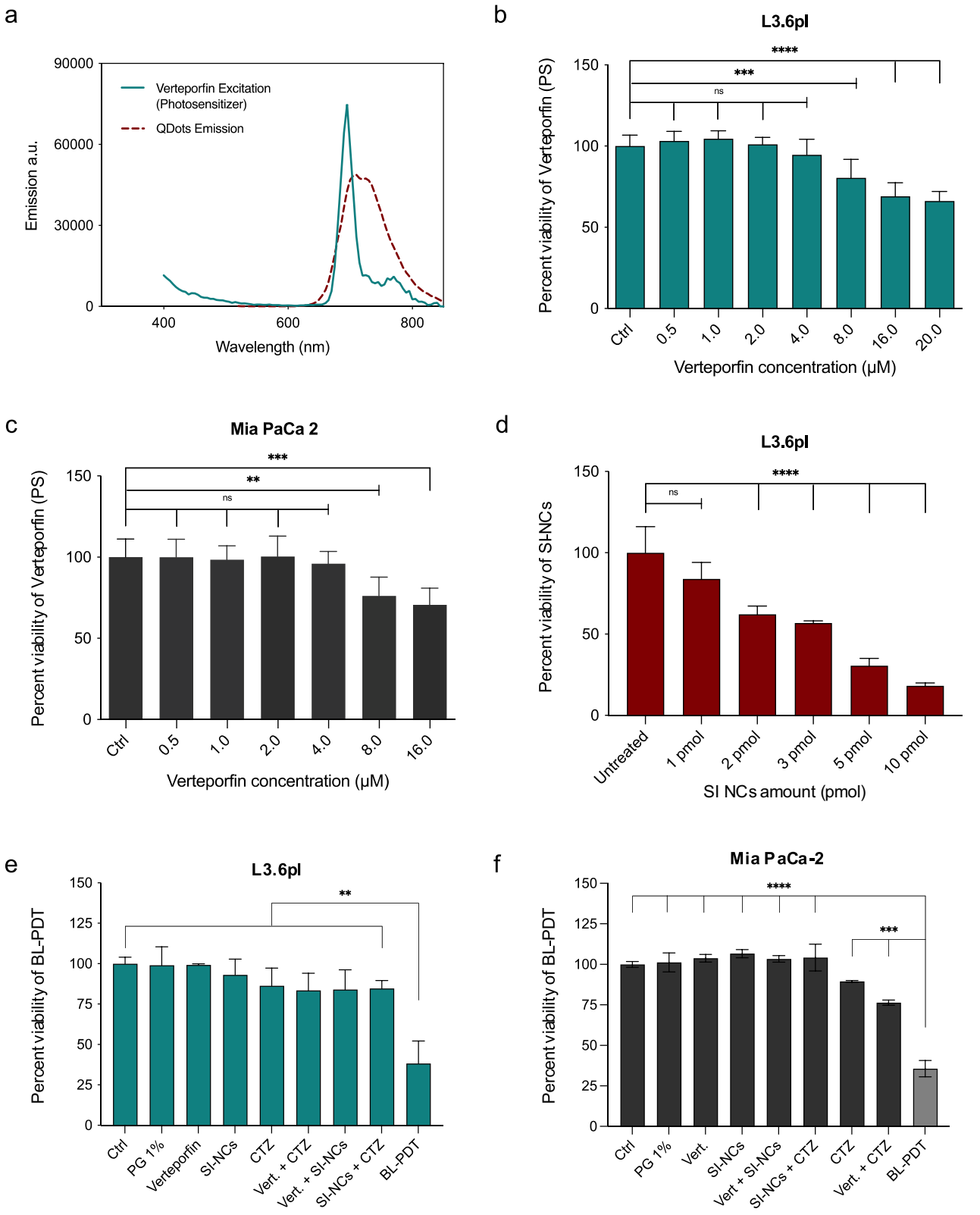

Figure 5 BL-PDT induces cell death in PDAC cells. (**a**) The excitation spectra of the photosensitizer matches the emission spectra of the QDots. Study of verteporfin cytotoxicity in (**b**) L3.pl6 and (**c**) Mia PaCa-2 cells after 4h of incubation at increasing concentrations (0–16 μM) of verteporfin. (**d**) SI-NCs cytotoxicity was evaluated by MTT in L3.6pl cells after 4h of incubation, with an IC_{50} calculated of 4.24 pmol. Statistical analyses: ANOVA with a Dunnett's test. Cell viability analysis following BL-PDT in (**e**) L3.6pl and (**f**) MiaPaCa-2 cells. Doses: Verteporfin (4 μM); SI-NCs (1 pmol); CTZ (20 μg/mL). Bars representing: 1–8 controls and 9 BL-PDT treatment. All data are expressed in terms of dose response and/or concentration/viability. Data are presented as means ± s.d. (at least n = 3 per group). Statistical analyses p-values: ns (non-significant) ** ($p < 0.01$), *** ($p < 0.001$) and **** ($p < 0.0001$).

https://doi.org/10.2147/IJN.S545161

The spectral overlap between verteporfin and QDots 705 (both in excitation and emission) validated their compatibility for our BL-PDT strategy.

We next evaluated verteporfin cytotoxicity in L3.6pl (Figure 5b), MiaPaCa-2 (Figure 5c), and in PANC-1 (Figure S4a) cells after 4h of incubation. As expected, cell death increased with increasing dosage in all lines, with no significant differences across them. Based on these results, 4 μM was selected as the working concentration, maintaining cell viability at 90–95%.

To assess potential baseline toxicity, we also tested SI-NCs alone in L3.6pl cells (Figure 5d). Due to the known cytotoxicity of QDots' heavy metal core, precise dose adjustment was required. The calculated IC_{50} was 4.24 μM (Figure S4b). Although some studies report IC_{50} values in the 100–400 nM range, this variability is influenced by QDot size, surface chemistry, core composition, cell type, and exposure time.[55]

Following the approach reported by *Kim* et al[30] we investigated whether BL-PDT could effectively induce cytotoxicity in PDAC cells. At an optimized low dose (1 pmol SI-NCs + 4 μM verteporfin), BL-PDT led to substantial cell death in both L3.6pl (Figure 5e) and MiaPaCa-2 (Figure 5f) cells. Importantly, no cytotoxicity was observed with individual components alone, including SI-NCs, verteporfin, CTZ, or its vehicle, 1% propylene glycol (PG).

We also examined the effect of higher SI-NC doses (5 pmol) on treatment efficacy. While higher SI-NC doses increased cytotoxicity in MiaPaCa-2, L3.6pl, and PANC-1 cells (Figure S4c–e), it also elevated nonspecific toxicity, highlighting the importance of dose optimization for therapeutic safety and selectivity.

BL-PDT-induced cytotoxicity is primarily mediated by reactive oxygen species (ROS), particularly singlet oxygen ($^1O_2$, SO), which can trigger apoptosis in cancer cells[7,17,56] To validate this mechanism in our system, we measured intracellular ROS levels using the fluorescent probe H_2DCFDA, and Luperox® (tert-butyl hydroperoxide; t-BHP) was included as an appropriate positive ROS-inducer control.[57] L3.6pl cells were pre-incubated with the dye and treated with BL-PDT as previously described, and a significant increase in ROS was detected 12 hours post-treatment.

A dose–response analysis was performed to determine the optimal SI-NC concentration for ROS generation (1–5 pmol per well). Maximum ROS levels were observed at 1–2 pmol of SI-NCs (Figure 6a). The same trend was confirmed in the PDX-derived Panc354 primary PDAC culture, which was also used for subsequent in vivo studies. Treatment with 2 pmol SI-NCs and 4 μM verteporfin effectively induced ROS without toxicity in control groups (Figure 6b).

Interestingly, ROS levels decreased at higher SI-NC doses (Figure 6a), suggesting that beyond a threshold, the mechanism underlying BL-PDT cell death may not be entirely ROS-dependent. This aligns with viability data indicating increased cytotoxicity at higher SI-NC concentrations, potentially implicating alternative cell death mechanisms such as necroptosis or necrosis.[58,59] This was further explored in subsequent in vivo studies described in the following sections.

We also compared the efficiency of BL-PDT to conventional laser-PDT. A custom-built laser emitting at 690 nm (photosensitizer activation wavelength) was used to irradiate L3.6pl cells pre-treated with verteporfin. Optimization experiments identified that a dose of 0.36 J/cm^2 (3 × 30s cycles) maximized ROS production (Figure S4f). At higher light doses, ROS-associated fluorescence decreased significantly, likely due to cellular damage activating alternative death pathways such as necrosis, paralleling our BL-PDT findings.[35,58]

Notably, BL-PDT using SI-NCs was more effective at ROS generation than laser-PDT under optimized conditions (Figure 6c), highlighting the superior potential of the bioluminescent approach.

To confirm that ROS generation leads to apoptosis, we used immunofluorescence staining for annexin V, a common apoptosis marker.[60] Confocal imaging showed strong annexin V staining only in BL-PDT-treated cells and the positive control (Figure 6d and Figure S5). These findings were corroborated by light microscopy, which revealed typical apoptotic morphology in treated L3.6pl cells (Figure 6e).

In summary, our in vitro data demonstrate that BL-PDT mediated by SI-NCs effectively induces ROS and promotes apoptosis in PDAC cells, validating its mechanism of action and therapeutic promise.

To assess the therapeutic efficacy of BL-PDT in vivo, we employed an orthotopic pancreatic tumor model using the Panc354 PDX cell line in male NOD.SCID mice. Mice were treated twice a week for 3 weeks, as outlined in the *Methods* section and supporting Figure S6. On the final treatment day, light emission from the SI-NCs was confirmed using an IVIS imaging system confirming successful tumor localization and activation approximately 45 minutes post-administration (30 min + 15 min) (Figure 7a). It is important to note that although our nanoconjugates lack an active targeting moiety, their accumulation within pancreatic tumors is likely mediated by the enhanced permeability and retention (EPR) effect, a mechanism similarly exploited by

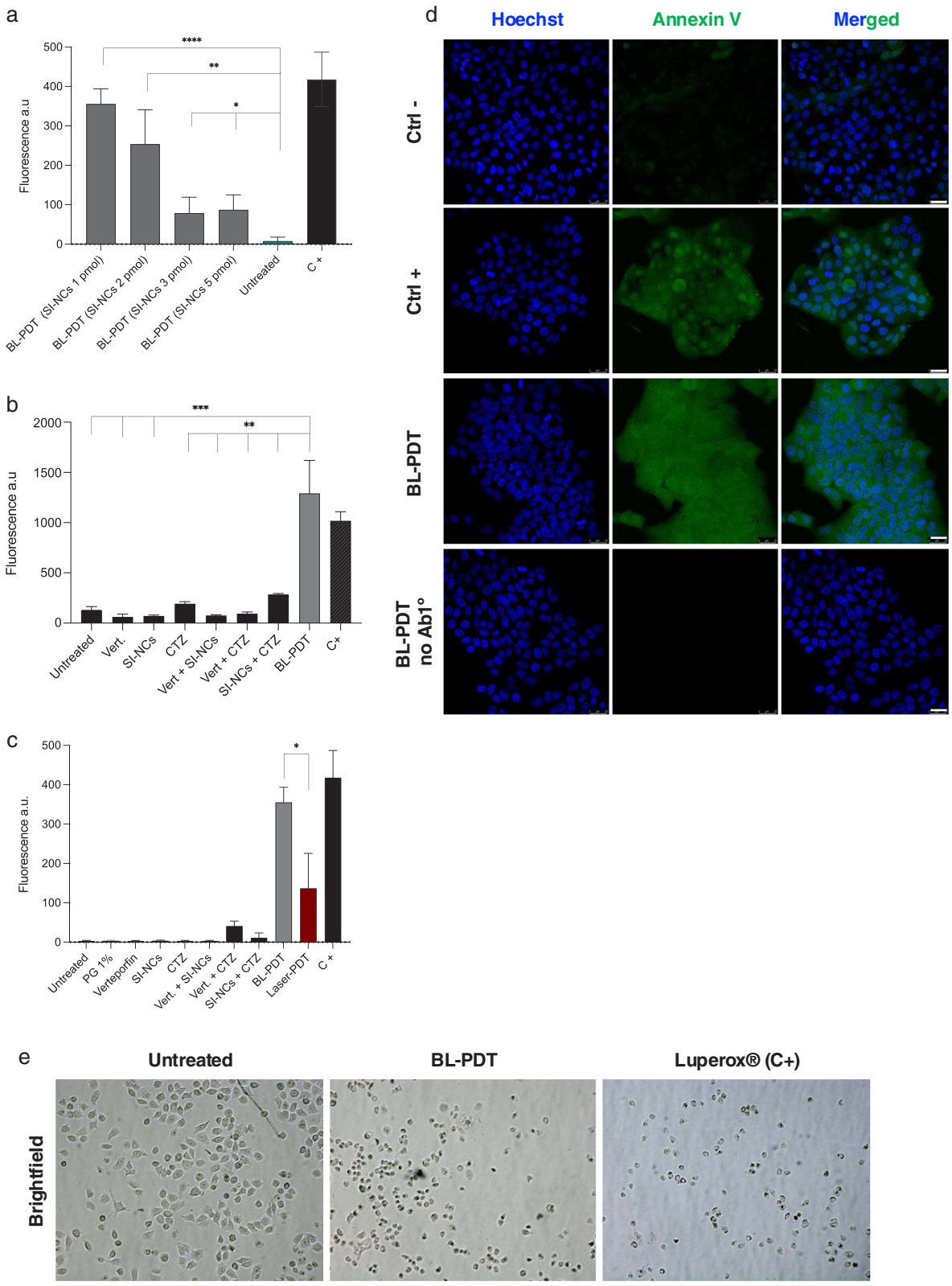

Figure 6 Ability of the SI-NCs to induce a therapeutic response. (**a**) H_2DCFDA assay to measure intracellular ROS levels in L3.6pl cells at increasing SI-NCs (1–5 pmol) doses. Best performance determined at 1 pmol treatment. (**b**) Intracellular ROS production, measured with the H_2DCFDA assay, in the pancreatic PDX-derived Panc354 primary culture, that will be further used for in vivo experiments. (**c**) Comparison of ROS generated with BL-PDT versus laser-PDT treatment. BL-PDTachieved a significant difference compared to laser-PDT in L3.6pl cells. (**d**) Confocal Laser Microscopy images of Annexin V levels assessed by IF to confirm the apoptosis cell-mediated killing mechanism after BL-PDT treatment. Appropriate negative controls and the positive control (Luperox®) were used to induce apoptosis. BL-PDT produced a higher Annexin V signal. (Scale bar: 25 µm, white). (**e**) Images of apoptotic cell morphology, observed by transmitted light microscopy after 16h BL-PDT treatment in L3.6pl cells. Data are presented as the mean ± s.d. (at least n = 3 per group). a.u. = arbitrary units. Statistical analyses p-value meaning: * ($p < 0.05$), ** ($p < 0.01$), *** ($p < 0.001$) and **** ($p < 0.0001$).

https://doi.org/10.2147/IJN.S545161

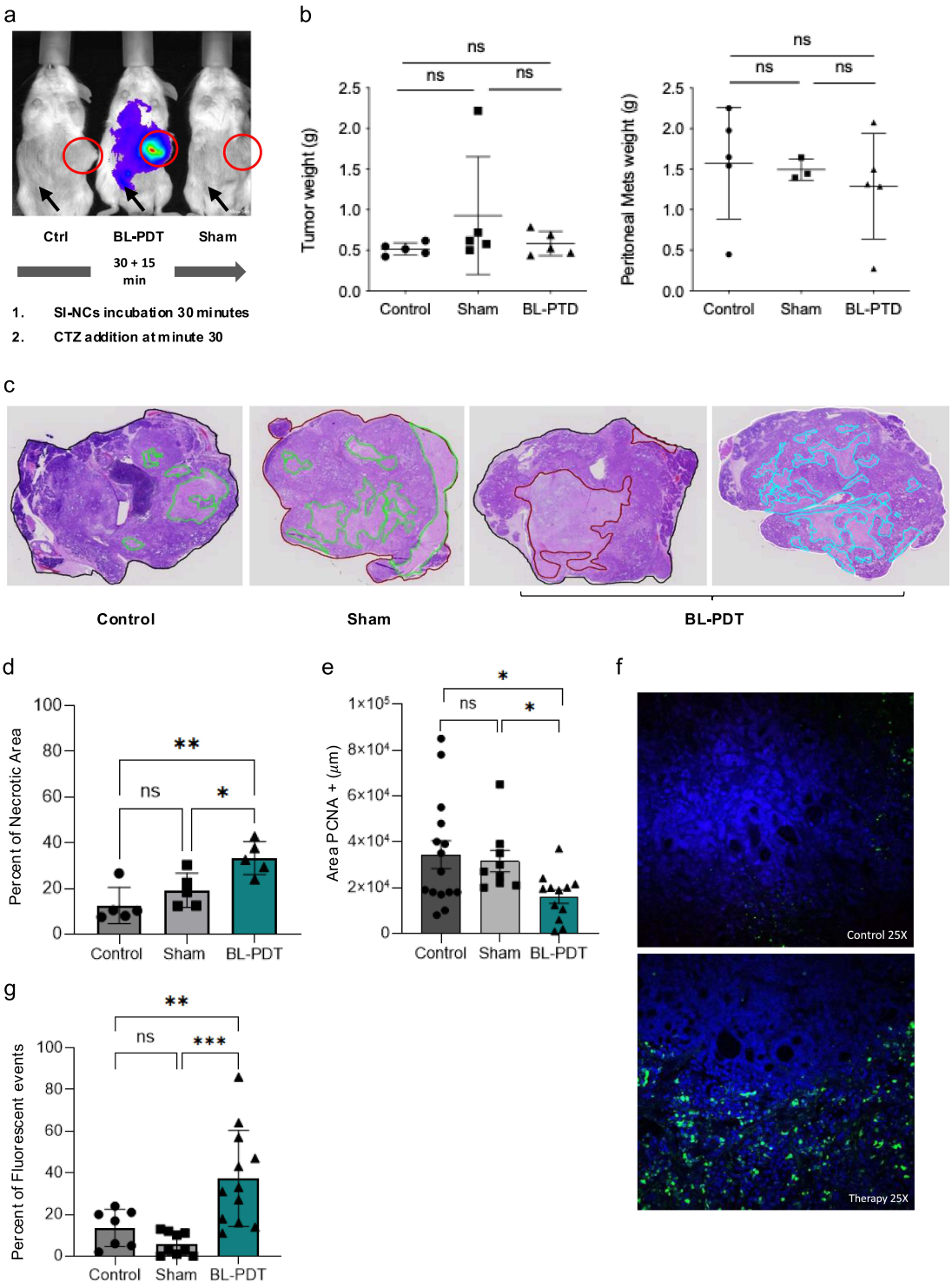

Figure 7 PDT treatment efficiently induces necrosis and apoptosis in Panc354PDX orthotopic tumors. (**a**) By IVIS analysis, SI-NCs (50 pmol i.p.) bioluminescence was observed at the tumor site (pancreas) 15 minutes after CTZ (5 nmol i.v.) injection. Images are shown for control (negative-control), sham (vehicle-control) and BL-PTD (positive-control) mice (n=5 mice per group). For the control group, PBS was injected. The therapy BL-PDT group consisted of mice treated with the complete BL-PDT treatment [verteporfin (PS) + SI-NCs + substrate (CTZ)]. The sham group consisted of mice treated with the photosensitizer and the SI-NCs without the substrate addition (no BL-PDT treatment). The black arrow indicates the site of injection, and the red circle marks the location of the tumor. (**b**) Mean ± s.d. of tumor (left) and peritoneal metastasis (right) weights in control, sham and BL-PTD groups, observing a tendency for reduction in the BL-PDT group. (**c**) Representative images of hematoxylin and eosin (H&E)-stained histological sections of tumors (3 μm) from the three experimental groups (control, sham and BL-PDT) from (**a**). (**d**) H&E-stained sections for each mouse were prepared, digitalized and used to evaluate the percentage of necrosis in the tumors. Data are presented as means ± s.d. of the % necrotic area/total tumor area. (**e**) Additional serial sections were used for IHC analysis of the number of PCNA-positive cells. Data are presented as means ± s.d. of the area of PCNA+ cells in representative sections from the control, sham and BL-PDT groups. (**f**) Apoptotic events in tumors were analyzed using the TUNEL assay, where images were captured by fluorescence microscopy. Nuclei were stained with Hoechst 33342 (blue), and TUNEL staining is shown in green (Zoom: 25X). (**g**) Positive green-fluorescent events for TUNEL were quantified in the control, sham and BL-PDT groups. Data are presented as means ± s.d. (at least n = 3 per group). Statistical analyses p-value meaning: ns (non-significant) * ($p < 0.05$), ** ($p < 0.01$).

https://doi.org/10.2147/IJN.S545161

other nanomedicines such as liposomal irinotecan (Onivyde®) and albumin-bound paclitaxel (Abraxane®). We acknowledge, however, that the highly desmoplastic and hypovascular nature of PDAC limits vascular permeability and increases interstitial pressure, thereby attenuating the classical EPR effect observed in other tumor types. Despite these barriers, clinically approved nanoformulations like Onivyde® and Abraxane® have demonstrated sufficient intratumoral accumulation and therapeutic efficacy in PDAC, likely through a combination of albumin-mediated transcytosis, stromal remodeling, and macrophage-mediated drug release. Therefore, while our approach likely relies primarily on passive tumor uptake, these precedents support the feasibility of nanoconjugate delivery in PDAC. Nevertheless, the restricted permeability of the PDAC stroma represents an important limitation that should be considered in translating this strategy to the clinical setting.

Although the present study was not designed as a comprehensive biodistribution and toxicology investigation, we performed a small pilot biodistribution experiment comparing intravenous and intraperitoneal administration of SI-NCs. Following intravenous injection, the relatively small hydrodynamic size of the nanoconjugates resulted in rapid renal clearance within a few hours and low tumor retention at later time points, making it difficult to complete the full therapeutic protocol within an optimal time window (data not shown). In contrast, intraperitoneal administration led to higher and more sustained accumulation of SI-NCs in orthotopic PDAC tumors, while still allowing sufficient time to administer verteporfin and CTZ. On this basis, intraperitoneal delivery was selected for the in vivo efficacy studies. Throughout these experiments, mice receiving both SI-NCs and verteporfin were closely monitored and did not exhibit overt signs of acute systemic toxicity (such as marked weight loss, abnormal behavior, or macroscopic organ damage at necropsy), supporting the notion that BL-PDT–induced damage was spatially restricted to the tumor region. Future work will be required to perform quantitative biodistribution analyses of both SI-NCs and verteporfin, together with more detailed toxicological assessments in appropriate models, to fully define the safety profile and therapeutic window of this approach.

Following sacrifice, therapeutic outcomes were evaluated. Although no statistically significant reduction in tumor weight was observed after three weeks of treatment (Figure 7b), a modest decrease in peritoneal metastases was noted in the treatment group, albeit without reaching significance. Histological analysis, however, revealed a marked increase in tumor necrosis in BL-PDT-treated animals compared to control and sham groups (Figure 7c). Quantification of necrotic areas (Figure 7d) confirmed that BL-PDT significantly increased tumor necrosis, indicating a clear cytotoxic effect despite unchanged tumor volume.

Proliferation was assessed by immunohistochemical staining for PCNA, a nuclear protein synthesized in the late G1 and S phases of the cell cycle. As shown, BL-PDT-treated tumors exhibited lower PCNA expression relative to controls, indicating reduced cell proliferation. However, this reduction did not reach statistical significance when compared to the sham group (Figure 7e).

To investigate the underlying mechanism of tumor cell death, apoptosis was evaluated via a TUNEL assay. Fluorescence microscopy of Panc354PDX tumors revealed a significant increase in TUNEL-positive (apoptotic) cells following BL-PDT treatment (Figure 7f), with quantification confirming a statistically significant elevation compared to controls (Figure 7g).

To validate these findings, we replicated the study in a second PDX model (PancA6LPDX), also established orthotopically in male NOD.SCID mice and treated under identical conditions (Figure S7a). The TUNEL assay again confirmed apoptosis induction in PancA6LPDX tumors (Figure S7b), with significantly higher apoptotic indices in BL-PDT-treated mice (Figure S7c).

Overall, these in vivo data demonstrate that BL-PDT can target PDAC tumor cells in the pancreas, inducing tumor cell death and apoptosis. While overall tumor mass remained unaffected, significant histological changes (increased necrosis, decreased proliferation, and enhanced apoptosis) confirmed the anti-tumoral activity of the treatment. A trend toward reduced peritoneal metastasis further supports the potential of BL-PDT, although statistical significance was not achieved.

While the overall approach validates the efficacy of BL-PDT in PDAC tumors, improvements are warranted. For example, a higher number of injections and an extended treatment regimen may have resulted in increased tumor cell death and a more profound and significant reduction in tumor and/or peritoneal metastasis weights in the BL-PDT group; however, the ethical endpoint was reached due to tumor burden in control animals. Use of immunocompetent or humanized mouse models could provide insight into immune-mediated clearance of necrotic and apoptotic cells following BL-PDT. Additionally, while 50 pmol of SI-NCs were administered, the precise quantity reaching tumor cells in vivo remains to be quantified for direct

comparison with in vitro efficacy. Combining BL-PDT with chemotherapy (eg., gemcitabine) might also enhance therapeutic outcomes. Despite these limitations, our data demonstrate that SI-NCs successfully generate intracellular bioluminescence to activate verteporfin and induce apoptosis in vivo across two PDAC PDX models.

This study supports the feasibility of using self-illuminating RLuc8–QDot705 nanoconjugates in combination with verteporfin as a promising strategy for treating PDAC. While our findings suggest that BL-PDT may circumvent some of the challenges associated with laser-PDT in deep or inaccessible tumors, a direct comparative study is necessary to substantiate this claim.[30]

Conclusion

This work introduces a self-illuminating nanoconjugate platform designed to overcome one of the fundamental barriers of photodynamic therapy: the limited penetration of externally applied light into deep-seated tumors such as PDAC. These nanoconjugates, composed of RLuc8 and QDot705, were engineered to activate the clinically approved photosensitizer verteporfin through BRET following the addition of the luciferase substrate CTZ. By enabling internal activation of an FDA-approved photosensitizer through bioluminescence, this approach offers a minimally invasive alternative to conventional laser-based PDT and expands its potential therapeutic reach.

Comprehensive in vitro analyses demonstrated that SI-NCs effectively internalize into multiple PDAC cell lines and, upon activation, induce robust ROS production and apoptosis, without the need for external light sources. In orthotopic PDAC PDX models, BL-PDT treatment induced significant histological changes, including increased tumor necrosis and apoptosis, confirming the in vivo therapeutic potential of this approach.

The proposed platform provides several advantages: (i) autonomous light generation that eliminates the need for optical fiber placement or external irradiation, (ii) compatibility with clinically used photosensitizers, and (iii) a modular nanoconjugate design that could be adapted to other therapeutic agents. However, important limitations remain, including restricted nanoparticle delivery within the dense PDAC stroma and the need for optimized dosing strategies to balance therapeutic efficacy with nanoparticle-associated toxicity. Future studies should address these challenges by improving tumor targeting, performing comprehensive biodistribution and toxicological analyses, and evaluating synergy with standard chemotherapeutic or immunomodulatory agents. Comparative studies against laser-PDT in vivo will also be valuable to validate the clinical advantages of this bioluminescent approach. In addition, long-term studies evaluating tumor recurrence, overall survival, pharmacokinetics and biodistribution, and the practical feasibility of integrating this platform into clinical workflows will be essential to fully assess its translational potential.

Taken together, these findings highlight the promise of SI-NCs as a nanotechnology-driven strategy to enable light-independent PDT for the treatment of deep-seated malignancies. While further optimization and direct comparative studies against laser-PDT are warranted, our results establish a foundation for the development of light-independent PDT strategies with the potential to broaden therapeutic options for PDAC and other deep or inaccessible tumors.

Supplementary Materials

The Supplementary Information document provides detailed descriptions of experimental methods, including reagent sources, protein purification procedures, quantum dot characterization, and laser system specifications. It also contains supplementary in vitro and in vivo data that support the findings of the main manuscript, such as electrophoresis results, spectral analyses, transmission electron microscopy (TEM) images, cellular uptake experiments, cytotoxicity assays, ROS production, apoptosis validation, and the full BioLight Photodynamic Therapy (BL-PDT) treatment protocol. Additional figures (S1– S7) illustrate these data to enhance reproducibility and offer further insight into the mechanisms and efficacy of the described nanoconjugate-based therapy.

Ethics Approval

All in vivo procedures involving animals were reviewed and approved by the *Comité de Ética de Experimentación Animal del Instituto de Investigaciones Biomédicas* "Alberto Sols" (IIB, CSIC-UAM), and by the Local Authorities (Comunidad de Madrid, PROEX 294/19). All animal procedures were conducted in strict accordance with Spanish

Government legislation (Real Decreto RD53/2013) and European Union directives (86/609/CEE, 2003/65/CE, and 2010/63/EU) on the protection of animals used for scientific purposes.

The use of patient-derived xenografts (PDX) was approved by the CSIC institutional review board with number 329/2024. Written informed consent was obtained from all participants or their legal guardians, and all procedures were conducted in accordance with the principles outlined in the Declaration of Helsinki.

PDAC patient-derived xenografts (Panc354 and PancA6L) were obtained from Dr. Manuel Hidalgo under a Material Transfer Agreement with the Spanish National Cancer Centre (CNIO), Madrid, Spain (Reference no. I409181220BSMH). This agreement includes confirmation that the original human tissue collection and PDX generation were conducted under appropriate ethical approval (*Comité de Ética del CNIO*), in compliance with applicable ethical standards.

All cell lines used are established and commercially available (ATCC).

Acknowledgments

This research has been funded by the Instituto de Salud Carlos III (ISCIII) through the grant AC18/00107 and co-financed the European Regional Development Fund (FEDER); by the ERA-NET EURONANOMED III project PANIPAC (grant number JTC2018/041 and PCI2019-103725). This study was also supported by the Biomedical Research Networking Center on Oncology (CIBERONC) (grant number ONC18PI04-NATBIL), and by Axencia Galega de Innovación grant number IN607B2024_14. M.A- S acknowledges the funding given by the Health Research Institute of Santiago de Compostela (IDIS) (predoctoral research fellowship/2020). We are also grateful to Professor Sanjiv Sam Gambhir M.D., PhD. (Stanford University) for the RLuc8 support in this study.

Disclosure

The authors declare the following competing financial interest(s): M.d.l.F. is the co-founder and CEO of DIVERSA Technologies SL. The remaining authors declare no conflict of interest.

All authors agree with the publication.

References

1. NCI. Available from: https://seer.cancer.gov/statfacts/html/pancreas.html. Accessed Apr 16, 2026.
2. Sung H, Ferlay J, Siegel RL, et al. Global Cancer Statistics 2020: GLOBOCAN Estimates of Incidence and Mortality Worldwide for 36 Cancers in 185 Countries. *CA Cancer J Clin*. 2021;71(3):209–249. doi:10.3322/caac.21660
3. Schouten TJ, van Goor IWJM, Dorland GA, et al. The Value of Biological and Conditional Factors for Staging of Patients with Resectable Pancreatic Cancer Undergoing Upfront Resection: a Nationwide Analysis. *Ann Surg Oncol*. 2024;31(8):4956–4965. doi:10.1245/s10434-024-15070-w
4. Hu JX, Lin YY, Zhao CF, et al. Pancreatic cancer: a review of epidemiology, trend, and risk factors. *World J Gastroenterol*. 2021;27(27):4298–4321. doi:10.3748/wjg.v27.i27.4298
5. Chen X, Zeh HJ, Kang R, Kroemer G, Tang D. Cell death in pancreatic cancer: from pathogenesis to therapy. *Nat Rev Gastroenterol Hepatol*. 2021;18(11):804–823. doi:10.1038/s41575-021-00486-6
6. Ackroyd R, Kelty C, Brown N, Reed M. The History of Photodetection and Photodynamic Therapy. *Photochemistry and Photobiology*. 2001;74(5):656–669. doi:10.1562/0031-8655(2001)074<0656:THOPAP>2.0.CO;2
7. Maharjan PS, Bhattarai HK. Singlet Oxygen, Photodynamic Therapy, and Mechanisms of Cancer Cell Death. *J Oncol*. 2022;2022:1–20. doi:10.1155/2022/7211485
8. Dos Santos AF, De Almeida DRQ, Terra LF, Baptista MS, Labriola L. Photodynamic therapy in cancer treatment - an update review. *J Cancer Metastasis Treat*. 2019;2019. doi:10.20517/2394-4722.2018.83.
9. Lee CN, Hsu R, Chen H, Wong TW. Daylight Photodynamic Therapy: an Update. *Molecules*. 2020;25(21):5195. doi:10.3390/molecules25215195
10. Zhen X, Cheng P, Pu K. Recent Advances in Cell Membrane–Camouflaged Nanoparticles for Cancer Phototherapy. *Small*. 2019;15(1). doi:10.1002/smll.201804105
11. Zhang Y, Wang B, Zhao R, Zhang Q, Kong X. Multifunctional nanoparticles as photosensitizer delivery carriers for enhanced photodynamic cancer therapy. *Materials Science and Engineering C*. 2020;115:111099. doi:10.1016/j.msec.2020.111099
12. Chen J, Fan T, Xie Z, et al. Advances in nanomaterials for photodynamic therapy applications: status and challenges. *Biomaterials*. 2020;237. doi:10.1016/j.biomaterials.2020.119827
13. Apel K, Hirt H. Reactive oxygen species: metabolism, oxidative stress, and signal transduction. *Annu Rev Plant Biol*. 2004;55(1):373–399. doi:10.1146/annurev.arplant.55.031903.141701
14. Steiling H, Munz B, Werner S, Brauchle M. *Different Types of ROS-Scavenging Enzymes Are Expressed during Cutaneous Wound Repair*. 1999. Available from: http://www.idealibrary.com. Accessed Apr 16, 2026.
15. Dąbrowski JM. Reactive Oxygen Species in Photodynamic Therapy: mechanisms of Their Generation and Potentiation. In: *Advances in Inorganic Chemistry*. Academic Press Inc.; 2017. Vol. 70:343–394. doi:10.1016/bs.adioch.2017.03.002
16. Parasca SV, Calin MA, Parasca SV. Photodynamic Therapy in Oncology. *J Optoelectron Adv Mater*. 2006; 8:1173.

17. Correia JH, Rodrigues JA, Pimenta S, Dong T, Yang Z. Photodynamic therapy review: principles, photosensitizers, applications, and future directions. *Pharmaceutics*. 2021;13(9):1332. doi:10.3390/pharmaceutics13091332
18. Yoon I, Li JZ, Shim YK. Advance in photosensitizers and light delivery for photodynamic therapy. *Clin Endosc*. 2013;46(1):7–23. doi:10.5946/ce.2013.46.1.7
19. Allison RR, Sibata CH. Oncologic photodynamic therapy photosensitizers: a clinical review. *Photodiagnosis Photodyn Ther*. 2010;7(2):61–75. doi:10.1016/j.pdpdt.2010.02.001
20. Zhao W, Wang L, Zhang M, et al. Photodynamic therapy for cancer: mechanisms, photosensitizers, nanocarriers, and clinical studies. *MedComm*. 2024;5(7). doi:10.1002/mco2.603
21. Ge M, Guo H, Zong M, et al. Bandgap-Engineered Germanene Nanosheets as an Efficient Photodynamic Agent for Cancer Therapy. *Angewandte Chemie - International Edition*. 2023;62(12):e202215795. doi:10.1002/anie.202215795
22. Zhang Y, Hao Y, Chen S, Xu M. Photodynamic Therapy of Cancers With Internal Light Sources: chemiluminescence, Bioluminescence, and Cerenkov Radiation. *Front Chem*. 2020;8:770. doi:10.3389/fchem.2020.00770
23. Algorri JF, Ochoa M, Roldán-Varona P, Rodríguez-Cobo L, López-Higuera JM. Light technology for efficient and effective photodynamic therapy: a critical review. *Cancers*. 2021;13(14):4384. doi:10.3390/cancers13143484
24. Grin M, Suvorov N, Ostroverkhov P, et al. Advantages of combined photodynamic therapy in the treatment of oncological diseases. *Biophys Rev*. 2022;14(4):941–963. doi:10.1007/s12551-022-00962-6
25. Hong EJ, Choi DG, Shim MS. Targeted and effective photodynamic therapy for cancer using functionalized nanomaterials. *Acta Pharm Sin B*. 2016;6(4):297–307. doi:10.1016/j.apsb.2016.01.007
26. Cui X, Zhang Z, Yang Y, Li S, Lee CS. Organic radical materials in biomedical applications: state of the art and perspectives. *Exploration*. 2022;2(2). doi:10.1002/EXP.20210264
27. So MK, Xu C, Loening AM, Gambhir SS, Rao J. Self-illuminating quantum dot conjugates for in vivo imaging. *Nat Biotechnol*. 2006;24(3):339–343. doi:10.1038/nbt1188
28. So MK, Loening AM, Gambhir SS, Rao J. Creating self-illuminating quantum dot conjugates. *Nat Protoc*. 2006;1(3):1160–1164. doi:10.1038/nprot.2006.162
29. Hsu CY, Chen CW, Yu HP, Lin YF, Lai PS. Bioluminescence resonance energy transfer using luciferase-immobilized quantum dots for self-illuminated photodynamic therapy. *Biomaterials*. 2013;34(4):1204–1212. doi:10.1016/j.biomaterials.2012.08.044
30. Kim YR, Kim S, Choi JW, et al. Bioluminescence-activated deep-tissue photodynamic therapy of cancer. *Theranostics*. 2015;5(8):805–817. doi:10.7150/thno.11520
31. Hamblin MR, Hasan T. Photodynamic therapy: a new antimicrobial approach to infectious disease? *Photochemical and Photobiological Sciences*. 2004;3(5):436–450. doi:10.1039/b311900a
32. Abrahamse H, Hamblin MR. New photosensitizers for photodynamic therapy. *Biochemical Journal*. 2016;473(4):347–364. doi:10.1042/BJ20150942
33. Visudyne.
34. Wei H, Wang F, Wang Y, et al. Verteporfin suppresses cell survival, angiogenesis and vasculogenic mimicry of pancreatic ductal adenocarcinoma via disrupting the YAP-TEAD complex. *Cancer Sci*. 2017;108(3):478–487. doi:10.1111/cas.13138
35. Huggett MT, Jermyn M, Gillams A, et al. Phase I/II study of verteporfin photodynamic therapy in locally advanced pancreatic cancer. *Br J Cancer*. 2014;110(7):1698–1704. doi:10.1038/bjc.2014.95
36. Lui JW, Xiao S, Ogomori K, Hammarstedt JE, Little EC, Lang D. The efficiency of verteporfin as a therapeutic option in pre-clinical models of melanoma. *J Cancer*. 2019;10(1):1–10. doi:10.7150/jca.27472
37. Ormond AB, Freeman HS. Dye sensitizers for photodynamic therapy. *Materials*. 2013;6(3):817–840. doi:10.3390/ma6030817
38. Li Y, Yu Y, Kang L, Lu Y. E*ffects of ChlorinE6-Mediated Photodynamic Therapy on Human Colon Cancer SW480 Cells*. *Int J Clin Experiment Med*. 2014;7:4867.
39. Sun X, Cao Z, Mao K, et al. Photodynamic therapy produces enhanced efficacy of antitumor immunotherapy by simultaneously inducing intratumoral release of sorafenib. *Biomaterials*. 2020;240:119845. doi:10.1016/j.biomaterials.2020.119845
40. Bruns CJ, Harbison MT, Kuniyasu H, Eue I, Fidler IJ. In Vivo Selection and Characterization of Metastatic Variants from Human Pancreatic Adenocarcinoma by Using Orthotopic Implantation in Nude Mice. *Neoplasia (New York, N.Y.)*. 1999;1(1):50–62. doi:10.1038/sj.neo.7900005
41. Möller J, Schroer MA, Erlkamp M, et al. The effect of ionic strength, temperature, and pressure on the interaction potential of dense protein solutions: from nonlinear pressure response to protein crystallization. *Biophys J*. 2012;102(11):2641–2648. doi:10.1016/j.bpj.2012.04.043
42. Mao XY, Tong PS, Gualco S, Vink S. Effect of NaCl addition during diafiltration on the solubility, hydrophobicity, and disulfide bonds of 80% milk protein concentrate powder. *J Dairy Sci*. 2012;95(7):3481–3488. doi:10.3168/jds.2011-4691
43. Koniev O, Wagner A. Developments and recent advancements in the field of endogenous amino acid selective bond forming reactions for bioconjugation. *Chem Soc Rev*. 2015;44(15):5495–5551. doi:10.1039/c5cs00048c
44. Burcham PC, Fontaine FR, Petersen DR, Pyke SM. Reactivity with Tris(hydroxymethyl)aminomethane Confounds Immunodetection of Acrolein-Adducted Proteins. *Chem Res Toxicol*. 2003;16(10):1196–1201. doi:10.1021/tx0341106
45. Ernst O, Zor T. Linearization of the Bradford protein assay. *Journal of Visualized Experiments*. 2010;(38). doi:10.3791/1918
46. Bhuckory S, Kays JC, Dennis AM. In vivo biosensing using resonance energy transfer. *Biosensors*. 2019;9(2):76. doi:10.3390/bios9020076
47. Couturier C, Deprez B. Setting up a bioluminescence resonance energy transfer high throughput screening assay to search for protein/protein interaction inhibitors in mammalian cells. *Front Endocrinol (Lausanne)*. 2012;3(SEP). doi:10.3389/fendo.2012.00100
48. Tyrosine R, Heteroreceptor K. Bioluminiscence Resonance Energy Transfer (BRET) Methods to Study G Protein-Coupled Recepror Complexes. *Methods in Cell Biology*. 2014;117:141–164. doi:10.1016/B978-0-12-408143-7.00008-6.BIOLUMINISCENCE
49. Dacres H, Michie M, Trowell SC. Comparison of enhanced bioluminescence energy transfer donors for protease biosensors. *Anal Biochem*. 2012;424(2):206–210. doi:10.1016/j.ab.2012.02.028
50. Xing Y, Kyung SM, Koh AL, Sinclair R, Rao J. Improved QD-BRET conjugates for detection and imaging. *Biochem Biophys Res Commun*. 2008;372(3):388–394. doi:10.1016/j.bbrc.2008.04.159
51. Tiwari DK, Tiwari M, Jin T. Near-infrared fluorescent protein and bioluminescence-based probes for high-resolution in vivo optical imaging. *Mater Adv*. 2020;1(5):967–987. doi:10.1039/d0ma00273a

52. Dragulescu-Andrasi A, Chan CT, De A, Massoud TF, Gambhir SS. Bioluminescence resonance energy transfer (BRET) imaging of protein-protein interactions within deep tissues of living subjects. *Proc Natl Acad Sci U S A*. 2011;108(29):12060–12065. doi:10.1073/pnas.1100923108
53. Li F, Yu J, Zhang Z, et al. Buffer enhanced bioluminescence resonance energy transfer sensor based on Gaussia luciferase for in vitro detection of protease. *Anal Chim Acta*. 2012;724:104–110. doi:10.1016/j.aca.2012.02.047
54. Cai W, Hsu AR, Li ZB, Chen X. Are quantum dots ready for in vivo imaging in human subjects? *Nanoscale Res Lett*. 2007;2(6):265–281. doi:10.1007/s11671-007-9061-9
55. Oh E, Liu R, Nel A, et al. Meta-analysis of cellular toxicity for cadmium-containing quantum dots. *Nat Nanotechnol*. 2016;11(5):479–486. doi:10.1038/nnano.2015.338
56. Fakhroueian Z, Dehshiri AM, Katouzian F, Esmaeilzadeh P. In vitro cytotoxic effects of modified zinc oxide quantum dots on breast cancer cell lines (MCF7), colon cancer cell lines (HT29) and various fungi. *Journal of Nanoparticle Research*. 2014;16(7). doi:10.1007/s11051-014-2483-2
57. Zhao W, Feng H, Sun W, Liu K, Lu JJ, Chen X. Tert-butyl hydroperoxide (t-BHP) induced apoptosis and necroptosis in endothelial cells: roles of NOX4 and mitochondrion. *Redox Biol*. 2017;11:524–534. doi:10.1016/j.redox.2016.12.036
58. Galluzzi L, Kepp O, Chan FKM, Kroemer G. Necroptosis: mechanisms and Relevance to Disease. *Annual Review of Pathology: Mechanisms of Disease*. 2017;12(1):103–130. doi:10.1146/annurev-pathol-052016-100247
59. Wang Y, Tang M. Dysfunction of various organelles provokes multiple cell death after quantum dot exposure. *Int J Nanomedicine*. 2018;13:2729–2742. doi:10.2147/IJN.S157135
60. Bastian AM, Yogesh TL, Kumaraswamy KL, Kumaraswamy KL. Various methods available for detection of apoptotic cells-A review. *Indian J Cancer*. 2013;50(3):274–283. doi:10.4103/0019-509X.118720